Biermann-battery driven magnetized collisionless shock precursors in laser produced plasmas

T. M. Johnson,* G. D. Sutcliffe, J. A. Pearcy, A. Birkel, G. Rigon, N. V. Kabadi, B. Lahmann, P. J. Adrian, B. L. Reichelt, J. H. Kunimune, S. G. Dannhoff, M. Cufari, and C. K. Li†
Plasma Science and Fusion Center, Massachusetts Institute of Technology, Cambridge, Massachusetts 02139, USA

F. Tsung
Department of Physics and Astronomy, University of California Los Angeles, Los Angeles, California 90095, USA

H. Chen
Lawrence Livermore National Laboratory, Livermore, California 94550, USA

J. Katz
Laboratory for Laser Energetics, University of Rochester, Rochester, New York 14623, USA

V. T. Tikhonchuk
Centre Lasers Intenses et Applications, University of Bordeaux, CNRS, CEA, 33405 Talence, France and The Extreme Light Infrastructure ERIC, ELI Beamlines Facility, 252 41 Dolní Břežany, Czech Republic
(Dated: February 27, 2025)

This letter reports the first complete observation of magnetized collisionless shock precursors formed through the compression of Biermann-battery magnetic fields in laser produced plasmas. At OMEGA, lasers produce a supersonic CH plasma flow which is magnetized with Biermann-battery magnetic fields. The plasma flow collides with an unmagnetized hydrogen gas jet plasma to create a magnetized shock precursor. The situation where the flowing plasma carries the magnetic field is similar to the Venusian bow shock. Imaging 2ω Thomson scattering confirms that the interaction is collisionless and shows density and temperature jumps. Proton radiographs have regions of strong deflections and FLASH magnetohydrodynamic (MHD) simulations show the presence of Biermann fields in the Thomson scattering region. Electrons are accelerated to energies of up to 100 keV in a power-law spectrum. OSIRIS particle-in-cell (PIC) simulations, initialized with measured parameters, show the formation of a magnetized shock precursor and corroborate the experimental observables.

Collisionless shocks are very common in astrophysical systems. Counter-streaming plasmas, ranging from Earth's magnetosphere[1] to relativistic astrophysical jets[2], often form shocks which dissipate energy. Charged particles can be accelerated to high energies inside shocks[3]. Magnetized shocks are one type of collisionless shock[4]. They form when a dynamically significant magnetic field is present in a system of counter-streaming plasmas and are very common in astrophysics[5]. The majority of planetary bow shocks, an example of a magnetized collisionless shock, form from the interaction between the weakly magnetized solar wind and a strongly magnetized planetary ionosphere[6]. Venus, however, has no magnetic field making the solar wind field responsible for its bow shock[7]. This is one astrophysical situation where the flowing plasma carries the magnetic field responsible for shock formation. Venus also has unexplained nightside aurorae which could be caused by charged particle acceleration in the bow shock[8].

This letter reports the first complete observation of a Biermann-battery driven magnetized collisionless shock precursor[9]. There are no externally imposed magnetic fields. Instead, Biermann-battery fields, generated during the laser drive, are frozen into the plasma flow. These fields are compressed in the collision between the plasma flow and gas jet plasmas. The magnetic field strength is enhanced, causing gas jet ions to be deflected and a magnetized shock precursor to be formed.

While magnetized shocks relevant to planetary bow shocks have been studied in the laboratory, all experiments have focused on the case where the stationary plasma contains the magnetic field[10–14]. The experiment presented here demonstrates a platform to study Venus's particular configuration where the flowing plasma carries the magnetic field. Such configurations have been studied previously, but the results lacked direct evidence of the magnetic field[15, 16]. Other experiments with a plasma flow colliding with a gas bag produced magnetized shocks, but the gas bag shell played a significant role in the overall physics of the experiment[17]. Additionally, the results of this experiment show that Biermann-battery generated magnetic fields can be strong enough to dominate the physics of laser-produced high-energy-density plasmas. This conclusion differs from studies of electromagnetic shocks with planar foils which found that Biermann-battery magnetic fields were not dynamically important to the overall interaction[18].

A schematic of the OMEGA experiment geometry is shown in Fig. 1. The gas jet produces a volume of hydrogen gas. Seven 351 nm laser beams each deliver 500 J of energy to a CH hemisphere in a 1 ns square pulse to produce a plasma flow. The gas jet volume is ionized prior to the arrival of the plasma flow[19]. The interaction between the gas jet plasma and the plasma flow is diagnosed with three diagnos-

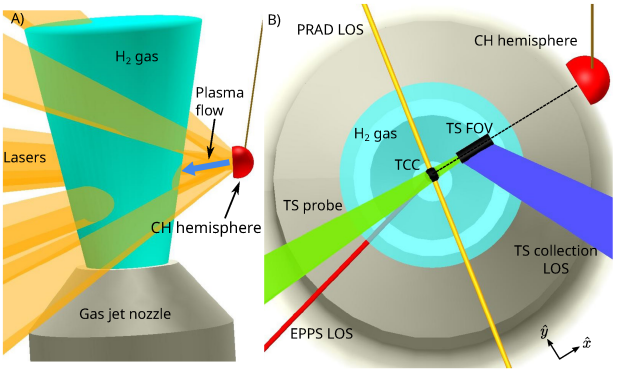

Figure 1. A) Side view of the OMEGA experimental configuration showing the gas jet, the hydrogen gas volume, and the CH hemispherical target. B) Detailed view showing the line-of-sight (LOS) for Thomson scattering (TS), proton radiography (PRAD), and electron spectroscopy (EPPS). TCC is at the center of the H_2 gas. The experimental x-axis goes from TCC to the CH target which is 7.5 mm away. The imaging Thomson field-of-view (FOV) is 1.5 mm long. In the experimental plane, the gas jet volume is ~ 3.7 mm in radius.

tics: Thomson scattering, proton radiography, and electron spectroscopy. The data from each of these diagnostics is discussed first while a complete physical picture is presented in the PIC simulation discussion.

Imaging 2ω Thomson scattering collects spatially resolved electron plasma wave (EPW) and ion acoustic wave (IAW) data at different times[20–22]. Analyzing these data produces profiles of electron density, electron temperature, and flow velocity at different time points. The Thomson probe beam points directly down the plasma flow axis and focuses to a region 2 mm from target chamber center (TCC). The probe beam delivers 10 J in a 100 ps square pulse while the spectrometer system has a frequency resolution of ~ 3 pixels for both EPW and IAW. The spatial field of view is ~ 1.5 mm in length along the probe beam with the scattering $\mathbf{k}$ vector 59.885 degrees off axis. Fig. 2 shows results from EPW and IAW measurements. All times reference the start of the laser drive on the hemispherical target.

Fig. 2 B) and C) show enhancements of the electron temperature and density due to the interaction between the gas jet and the plasma flow. Comparing the location of the density jump across different times shows that the feature has a velocity of 1000 ± 200 km/s. The width of the density peak at 4.5 ns is ~ 300 μm (compared to ion skin-depth, ~ 100 μm, and Larmor radius, ~ 500 μm, see PIC simulations).

Fig. 2 D) shows the raw IAW spectrum which contains two plasma species. The spectrum centered around the probe wavelength is the gas jet plasma since it is stationary. Blue shifted from the probe is the plasma flow spectrum. Its velocity is close to the velocity of just the plasma flow, but with a localized velocity dip seen in Fig. 2 E).

Flow velocity measurements of the plasma flow confirm low ion-ion collisionality. For the plasma flow only at 4.5 ns, the velocity exceeds 1500 km/s as seen in Fig. 2 E). The velocity increases farther away from the CH hemisphere target[23, 24]. With flow velocity and density measurements, the interspecies ion-ion collision mean-free-path can be calculated:

$$\lambda_{\mathrm{mfp}} = \frac{(4\pi\varepsilon_0)^2}{n_2 Z_1^2 Z_2^2 e^4} \frac{m_1 m_2 v_1^4}{8\pi \log\Lambda} \tag{1}$$

where indices 1 (2) refers to the plasma flow (gas jet), n is the ion density, Z is the charge state, m is the ion mass, and $\log\Lambda$ is the Coulomb logarithm[25]. For the experiment, the plasma flow carbon ion mean-free-path is about 7 cm which is much larger than both the system size making the interaction interspecies ion-ion collisionless.

Fig. 2 F) shows time resolved measurements of ZT_e for the gas jet plasma in front of the density jump. The red box in Fig. 2 D) shows the region where ZT_e is measured. The ZT_e values agree with the EPW measured T_e values in front of the temperature peak ($Z = 1$ for hydrogen). This heating is caused by electron-ion collisional friction[24]. Such heating is largely spatially uniform and does not explain the observed localized shock precursor temperature jump[19].

The density jumps by 2.53 ± 0.15 times (compared the gas jet density of 5.7×10^{18} cm^{-3}) and the temperature jumps by 1.94 ± 0.12 times (at 4.5 ns, the gas jet has been heated to about 350 eV). These jumps are measured with respect to the gas jet. The measured jumps do not match the Rankine-Hugoniot conditions for the sonic Mach number of ~ 4[19]. This is because the interaction is only a shock precursor[26]. At the probed time, the shock is still developing as seen in Fig. 2 C) where the density peak increases with time.

Proton radiography images the electromagnetic fields from the plasma flow gas jet interaction[27, 28]. Lasers implode a D^3He capsule to produce protons at 3 and 15 MeV to probe the plasma. Fig. 3 A) shows a resulting 3 MeV radiograph. The radiograph has a region of strong deflection co-located with the Thomson scattering region. There are few filaments at the probed time meaning that the large deflections cannot be from the Weibel instability (see appendix)[18]. The only other source of fields are Biermann-battery fields from the laser drive. 2D PIC simulations of similar configurations show separation between Biermann and filamentary fields[29]. Deflections from electric fields can be ruled out[19].

A Monge-Ampere method reconstructs the path-integrated magnetic field which produced the radiographs[30]. Fig. 3 B) and C) show the field perpendicular and parallel to the plasma flow, respectively. The perpendicular field has a region of strong positive and negative fields. The parallel field is weak and filamentary, having a root-means-square average magnitude five times weaker than the perpendicular field. This further supports the claim that the Weibel instability is not important for the dynamics of the interaction.

A simple toroidal magnetic field is able to create radiographs similar the experimental in Fig. 3 A). This model is similar to the expected geometry for Biermann-battery fields

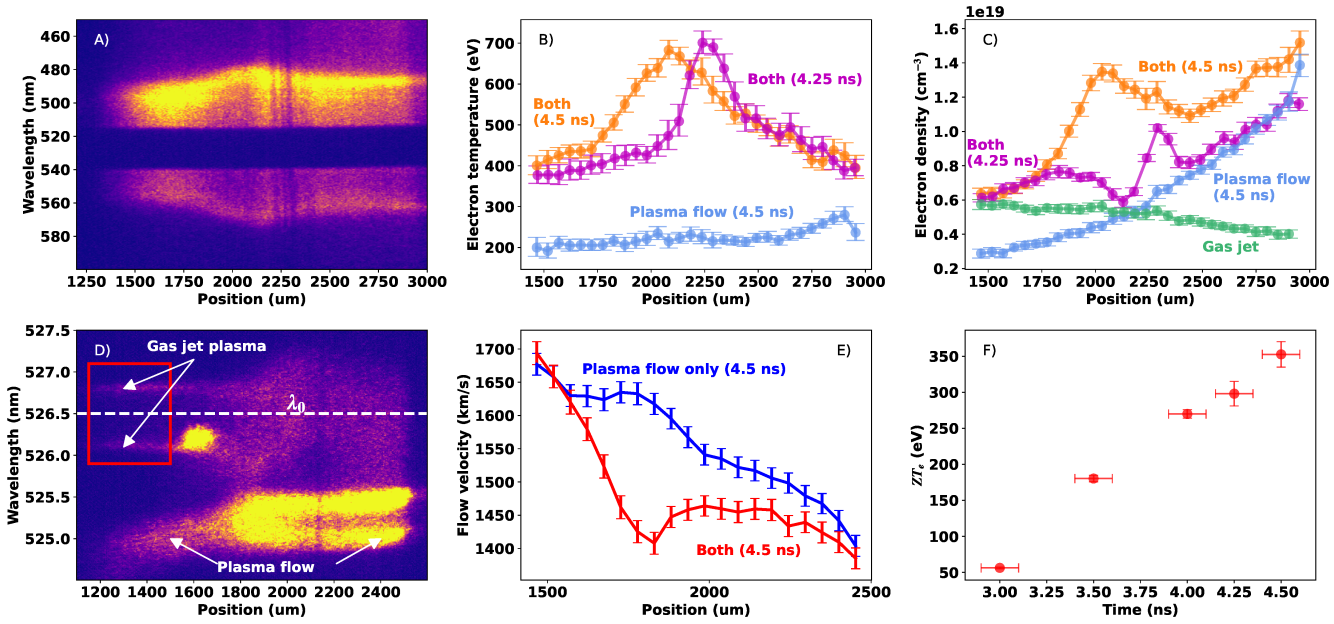

Figure 2. Thomson scattering results where $t = 0$ references the start of the laser drive. A) Thomson EPW spectrum at 4.5 ns for shots with both the gas jet and the plasma flow. Distance is measured away from TCC along the plasma flow axis. B) Electron temperature profiles for the interaction at different times compared to a plasma flow only shot. C) Electron density profiles for the interaction compared to the plasma flow and gas jet profiles. D) Thomson IAW spectrum at 4.5 ns showing the gas jet plasma spectrum around the probe wavelength and the blue shifted plasma flow spectrum. E) Flow velocity profile at 4.5 ns for shots with and without the gas jet. F) Time resolved and spatially averaged (from red box region in D) ZT_e of the gas jet plasma ahead of the shock.

generated in plasma bubbles[31]. Consider a simple magnetic vector potential:

$$A_x = \frac{B_0 a}{2} \exp\left(-\frac{r^2}{a^2} - \frac{x^2}{b^2}\right) \tag{2}$$

where a is the field structure radius, b is the thickness, B_0 is the field strength, and r is the radius from the origin[31]. Fig. 3 D) shows a synthetic radiograph generated with a proton tracing code probed 10° off-axis, the same as the experiment. The resulting synthetic radiograph is similar to the experimental data. Reconstructing the synthetic radiograph produces strong fields perpendicular to the x-axis, the plasma flow axis. This analysis shows that the radiograph's strong deflection region is consistent with Biermann-battery fields.

A set of 3D Cartesian FLASH ideal MHD simulations with the Biermann-battery term model the plasma flow Biermann fields before the collision with the gas jet[32, 33]. These simulations have the same laser configuration as in the experiment with the target shifted a realistic 50 μm in the y-direction. The simulation results in Fig. 3 F) show the magnetic field topology. Biermann fields are present along the plasma flow axis and therefore are present in the Thomson scattering volume, located 1.75 mm outside the simulation domain. A roughly toroidal region can be seen in the highlighted regions in Fig. 3 F). When compressed, these fields increase in magnitude and produce the radiographs in Fig. 3 A).

Electron spectroscopy measurements, using the Electron Positron Proton Spectrometer (EPPS) diagnostic[34, 35], show the acceleration of electrons into a high energy power-law spectrum. EPPS uses a 0.03 T magnet to deflect electrons onto an imageplate and is time integrated. To find the net acceleration spectrum, shots with and without the gas jet are compared in Fig. 4 A). The resulting spectrum is shown in Fig. 4 B). A Maxwellian with the maximum measured electron temperature is fit to the low energy part of the spectrum to emphasize the high energy tail. A power-law is fit to the high energy non-thermal part of the spectrum yielding a spectral index of -3.6 and giving clear evidence of electron acceleration. A simple r^2 analysis confirms the quality of the fit. Stimulated Raman scattering from the laser passing through the gas jet is ruled out as a source of fast electrons[19].

Particle-in-cell (PIC) simulations are performed to study the kinetic aspects of the interaction. OSIRIS 1D3V PIC simulations show the formation of a magnetized shock precursor for experimentally relevant conditions[36]. The PIC simulations span 6000 μm of space with $dx = 0.034$ μm and have 1000 particles per cell and realistic mass ratios. Fig. 5 A) shows the initial conditions of the simulation with a uniform density profile on the left for the gas jet plasma and a self-similar density profile on the right for the plasma flow. Part of the plasma flow has a uniform magnetic field of 75 kG with an associated induction electric field to model the Biermann-battery fields. The left (gas jet) plasma is stationary while the

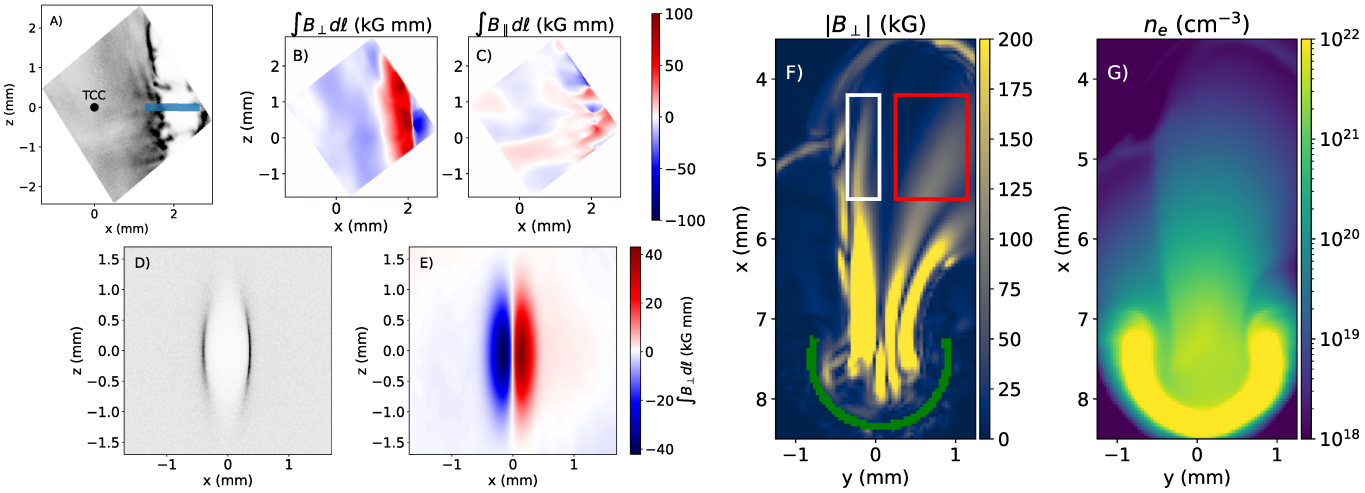

Figure 3. A) 3 MeV proton radiograph taken at 5.1 ns after the laser drive starts showing a sharp deflection region of strong field. The blue region shows the Thomson scattering volume projected into the radiograph field-of-view. B) and C) show the reconstructed path-integrated magnetic field perpendicular and parallel to the flow direction, respectively. D) Synthetic radiograph generated by probing equation 2 10° off axis with $B_0 = 350$ kG, $a = 0.08$ cm, and $b = 0.0175$ cm. E) Reconstruction of the synthetic radiograph. F) and G) show 2D slices of the magnetic field magnitude perpendicular to the plasma flow and the electron density, respectively, from FLASH simulations. The green shows the hemisphere target. The regions inside the white and red rectangles combine to create a toroidal magnetic field. Note that the gas jet plasma, located ~ 3.7 mm from TCC, is not in the simulation domain.

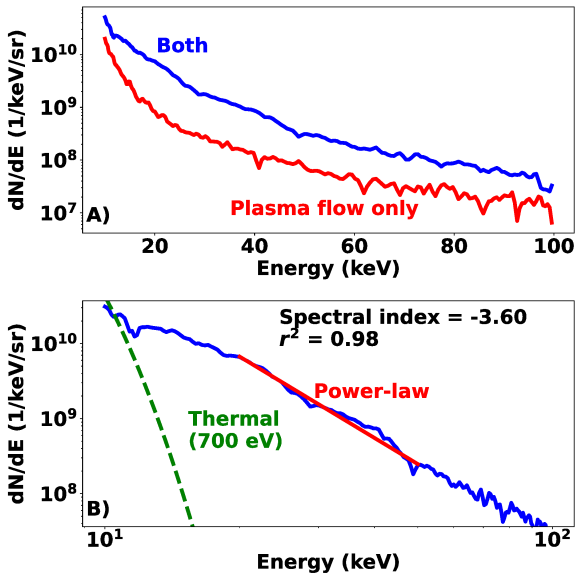

Figure 4. A) Electron spectra from a shot with the interaction and a plasma flow only shot. B) Log-log plot of the net electron spectrum. A fixed temperature Maxwellian is fit to the low energy emphasizing the non-thermal nature of the spectrum. A power-law is fit to the high energy portion of the spectrum.

right (plasma flow) plasma flows into it with a velocity profile similar to Fig. 2 E).

The simulation captures essential features of magnetized shock precursor formation. Here, time $t = 0$ references the initial interpenetrate of the plasma flow with the gas jet which occurs at about 3 ns in the experiment. Since the ions are collisionless, the plasma flow ions pass through the interface, increasing the total density. The magnetic field reflects the gas jet electrons meaning that the plasma flow electrons alone neutralize the ion charge, causing an increase in the plasma flow electron density. Since the magnetic field is frozen into the plasma flow (magnetic Reynolds number ~ 380), the increase in the plasma flow electron density also increases the magnetic field strength to around 225 kG. Magnetic flux conservation requires that the magnetic field peak propagates forward slower than the initial plasma flow velocity. Simply put, the system forms a magnetized piston immediately after the collision[29]. Fig. 5 B) shows the profiles after the simulation has evolved. The magnetic field is strong enough to start deflecting the gas jet ions (gyro-radius ~ 500 μm), seen in Fig. 5 C), increasing the ion density and moving the density peak away from the interface at a velocity of 950 km/s. Plasma flow ions have larger q/m compared to the gas jet ions, making them stiffer to deflection and causing the plasma flow density to be largely unaffected by the field.

The electric field is enhanced less than the magnetic field resulting in a net Lorentz force on the plasma flow ions in the field region. This causes the plasma flow ions to accrue velocity in the y-direction. The Thomson IAW Doppler shift is sensitive to $\mathbf{k} \cdot \mathbf{v}$. In the experimental geometry, the angle between the probe $\mathbf{k}$ vector and the plasma flow axis is $\theta \sim 60°$ causing the Doppler shift to be effected by v_y:

$$\mathbf{k} \cdot \mathbf{v} = (k_i - k_s \cos(\theta)) v_x - k_s \sin(\theta) v_y, \tag{3}$$

where k_i and k_s are the magnitudes of the probe and collected light wavevectors. Fig. 5 D) shows the Doppler shift with

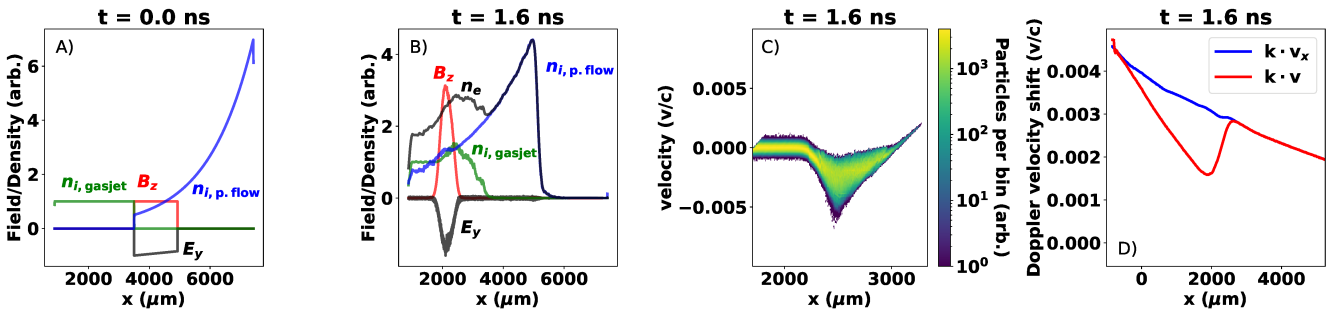

Figure 5. A) Initial simulation EM field and density profiles. B) Simulation profiles at $t = 1.59$ ns. C) Gas jet ion x-velocity x-position phase space plot at $t = 1.59$ ns. D) Thomson scattering-like Doppler shift of the plasma flow ions from deflection in the magnetic field. The localized dip is consistent with Fig. 2 E). In all plots, the x axis references distance from TCC.

a localized dip due to plasma flow ion deflections which is consistent with the experimental IAW velocity measurements shown in Fig. 2 E). Deflected gas jet ions are outshone by the higher-Z plasma flow ions[20].

The PIC simulations results match the experimental measurements well. The velocities of the magnetic field and the density jump are measured in the simulation to be 870 km/s and 950 km/s respectively, which is comparable to the experimentally measured velocity of 1000 ± 200 km/s. The simulated density profile has a similar shape and peak value compared to the EPW measurements. Deflections of the plasma flow ions produce similar Doppler shifts as the Thomson IAW data. With the initial simulation magnetic field of 75 kG and the gas jet density ($n_e = 5.7 \times 10^{18}$ cm^{-3}), the magnetized precursor has an Alfvén Mach number of $M_A \sim 14$ making it supercritical[5].

The measured electron acceleration is not seen in the PIC simulations, likely due to limitations of the 1D simulation. Given the enhanced magnetic field strength of ~ 200 kG, different shock acceleration mechanisms can be considered. The electron gyro-radius is too small for diffusive shock acceleration[37] and the Alfvén Mach number is too small for shock surfing acceleration[38]. The last mechanism left is shock drift acceleration (SDA) where electrons traveling along the magnetic field ramp are accelerated by the induction electric field[39]. The observed acceleration is therefore plausibly attributed to SDA.

The observed shock precursor differs from previous experiments since it moves slower than the initial flow velocity[10, 11]. Viewed from the center-of-mass frame, the shock precursor is moving backwards towards the CH target. If fully formed, the shock would be the reverse shock. Given enough time and energy, a forward moving electromagnetic shock could form via the beam-Weibel instability[29].

In summary, this letter presents the first complete observation of magnetized collisionless shock precursors in laser-driven plasmas without externally imposed magnetic fields. The experiment offers a laboratory example of the formation of Venus's bow shock. Unlike many planets in the solar system, Venus lacks a global magnetic field. The flowing solar wind carries the magnetic field responsible for shock formation. Table I compares dimensionless parameters between the experiment and Venus[41]. These numbers compare favorable indicating that the same physics is taking place. The observed electron acceleration could be relevant to the unknown origin of the nightside aurorae on Venus.

Table I. Comparison of dimensionless parameters for Venus and the experiment[6, 40].

Parameter	Venus	Experiment
$\mathscr{M}_s$	~ 5.1	4.1
β_e	1.4	2.0
Re	8.75×10^{11}	4.18×10^5
Re_M	2.85×10^{15}	3.8×10^2
Pm	3.07×10^{-4}	9.1×10^{-3}

This work was supported, in part, by the U.S. Department of Energy NNSA MIT Center-of-Excellence under Contract No. DE-NA0003868, by the National Laser Users Facility under Contract No. DE-NA0003938, and by the NNSA HEDLP program under Contract No. DE-NA0004129. Some of the simulations presented in this paper were performed on the MIT-PSFC partition of the Engaging cluster at the MGHPCC facility (www.mghpcc.org) which was funded by DoE grant number DE-FG02-91-ER54109. The software used in this work was developed in part by the DOE NNSA and DOE Office of Science-supported Flash Center for Computational Science at the University of Chicago and the University of Rochester. The authors acknowledge the OSIRIS Consortium, consisting of UCLA and IST (Portugal) for the use of the OSIRIS 4.0 framework. This research used resources of the National Energy Research Scientific Computing Center (NERSC), a U.S. Department of Energy Office of Science User Facility located at Lawrence Berkeley National Laboratory, operated under Contract No. DE-AC02-05CH11231 using NERSC award m1157. The authors would like to thank the OMEGA operations team for supporting this experiment as well as R. Frankle and E. Doeg for processing the CR-39. The authors also thank W. Fox, D. Schaeffer, P. Tzeferacos,

and A. Milder for helpful discussions and the peer-review referees for their insightful comments.

APPENDIX

The interpenetration of the plasma flow with the hydrogen gas jet plasma makes the interaction clearly beam-Weibel unstable[42, 43]. Despite this fact, the region of strong deflection does not arise because of the Weibel instability. Figure 6 shows a time series of proton radiographs. At 4.8 ns, the earliest time radiography, there are hardly any filaments in front of the region of strong deflection. As time goes on, it is clear that filaments start to emerge. The region of strong deflection is most important to the discussion in the main text. The emergence of filaments over about 1 ns of time is consistent with the Weibel growth time of $\sim .4$ ns[44].

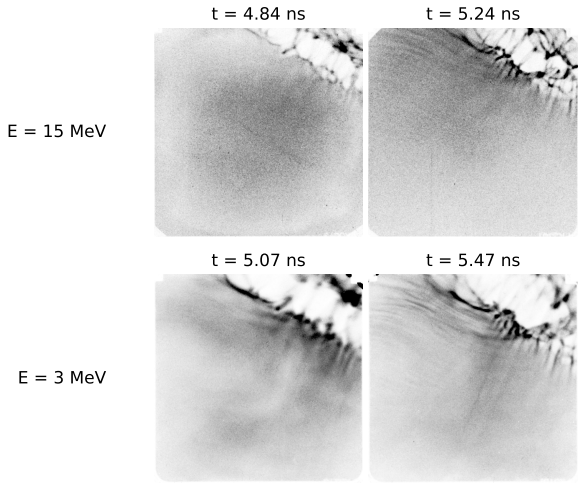

Figure 6. Proton radiographs taken at different times and at different energies. Note that there are very few filaments early in time. As time goes on, filaments appear more clearly.

The region of strong deflection is therefore not caused by the Weibel instability. As seen in the FLASH simulations shown in Figure 3 of the main text, there are strong Biermann-battery magnetic fields at the outer edge of plasma flow. This means that the magnetic field responsible for the strong deflection comes from Biermann-battery fields. The filaments only emerge ($t > 5$ ns) after the physics of the shock precursor formation occurs as detailed by Thomson scattering measurements ($t < 4.5$ ns) the in the main text.

* tmarkj@mit.edu
† ckli@mit.edu

[1] F. S. Mozer, Geophys. Res. Lett. **8**, 823 (1981).
[2] M. V. Medvedev and A. Loeb, Astrophys. J. **526**, 697 (1999).
[3] M. Ackermann et al., Science **339**, 807 (2013).
[4] Y. Sakawa, T. Morita, Y. Kuramitsu, and H. Takabe, Adv. Phys. X. **1**, 425 (2016).
[5] R. A. Treumann, Astron. Astrophys. Rev. **17**, 409 (2009).
[6] A. Balogh and R. A. Treumann, *Physics of collisionless shocks*, ISSI Scientific Report Series, Springer, New York, NY, 2013 edition, 2013.
[7] J. G. Luhmann, Space Sci. Rev. **44** (1986).
[8] S. A. Kovac et al., Astrophys. J. **929**, 45 (2022).
[9] L. Biermann and A. Schlüter, Phys. Rev. **82**, 863 (1951).
[10] D. B. Schaeffer et al., Phys. Rev. Lett. **119**, 025001 (2017).
[11] D. B. Schaeffer et al., Phys. Rev. Lett. **122**, 245001 (2019).
[12] W. Yao et al., Nature Physics **17**, 1177 (2021).
[13] F. Suzuki-Vidal et al., Astrophys. J. **815**, 96 (2015).
[14] J. M. Levesque et al., Phys. Plasmas **29**, 012106 (2022).
[15] R. Yamazaki et al., Phys. Rev. E. **105**, 025203 (2022).
[16] T. Umeda et al., Phys. Plasmas **26**, 032303 (2019).
[17] C. K. Li et al., Phys. Rev. Lett. **123**, 055002 (2019).
[18] C. M. Huntington et al., Nat. Phys. **11**, 173 (2015).
[19] See Supplemental Material at `https://link.aps.org`, which includes Refs. [24, 26, 27, 45–50] for more details.
[20] J. Sheffield, D. Froula, S. H. Glenzer, and N. C. Luhmann, Jr, *Plasma scattering of electromagnetic radiation*, Academic Press, San Diego, CA, 2 edition, 2010.
[21] J. Katz, J. S. Ross, C. Sorce, and D. H. Froula, Journal of Instrumentation **8** (2013).
[22] J. Katz et al., Rev. Sci. Instrum. **83**, 10E349 (2012).
[23] P. Mora, Phys. Rev. Lett. **90**, 185002 (2003).
[24] J. S. Ross et al., Physics of Plasmas **19**, 056501 (2012).
[25] H.-S. Park et al., High Energy Density Phys. **8**, 38 (2012).
[26] D. B. Schaeffer et al., Phys. Plasmas **27**, 042901 (2020).
[27] C. K. Li et al., Rev. Sci. Instrum. **77**, 10E725 (2006).
[28] C. K. Li et al., Phys. Rev. Lett. **100**, 225001 (2008).
[29] Q. Moreno et al., Phys. Plasmas **27**, 122106 (2020).
[30] A. F. A. Bott et al., J. Plasma Phys. **83** (2017).
[31] N. L. Kugland, D. D. Ryutov, C. Plechaty, J. S. Ross, and H.-S. Park, Rev. Sci. Instrum. **83**, 101301 (2012).
[32] B. Fryxell et al., Astrophys. J. Suppl. Ser. **131**, 273 (2000).
[33] P. Tzeferacos et al., High Energy Density Phys. **17**, 24 (2015).
[34] H. Chen et al., Rev. Sci. Instrum. **79**, 10E533 (2008).
[35] H. Chen et al., Rev. Sci. Instrum. **79**, 033301 (2008).
[36] R. A. Fonseca et al., Osiris: A three-dimensional, fully relativistic particle in cell code for modeling plasma based accelerators, in *Computational Science — ICCS 2002*, edited by P. M. A. Sloot, A. G. Hoekstra, C. J. K. Tan, and J. J. Dongarra, pages 342–351, Berlin, Heidelberg, 2002, Springer Berlin Heidelberg.
[37] A. R. Bell, Mon. Not. R. Astron. Soc. **182**, 147 (1978).
[38] Y. Matsumoto, T. Amano, and M. Hoshino, Astrophys. J. **755**, 109 (2012).
[39] C. S. Wu, J. Geophys. Res. **89**, 8857 (1984).
[40] C. T. Russell, J. G. Luhmann, and R. J. Strangeway, Planet. Space Sci. **54**, 1482 (2006).
[41] D. D. Ryutov, R. P. Drake, and B. A. Remington, Astrophys. J. Suppl. Ser. **127**, 465 (2000).
[42] E. S. Weibel, Phys. Rev. Lett. **2**, 83 (1959).
[43] T. N. Kato and H. Takabe, Phys. Plasmas **17**, 032114 (2010).
[44] H.-S. Park et al., Phys. Plasmas **22**, 056311 (2015).
[45] J. D. Huba, *NRL PLASMA FORMULARY Supported by The Office of Naval Research*, Naval Research Laboratory, Washington, DC, 2013.
[46] F. F. Chen, *Introduction to plasma physics and controlled fusion*, Springer International Publishing, Cham, Switzerland, 3 edition, 2015.

[47] D. W. Forslund and C. R. Shonk, Phys. Rev. Lett. **25**, 1699 (1970).
[48] C. Thoma, D. R. Welch, R. E. Clark, D. V. Rose, and I. E. Golovkin, Phys. Plasmas **24**, 062707 (2017).
[49] K. Estabrook and W. L. Kruer, Phys. Fluids **26**, 1892 (1983).
[50] A. S. Davies et al., Phys. Rev. Lett. **122**, 155001 (2019).